# Feasibility of spiral fMRI based on an LTI gradient model

Nadine N. Graedel[1,2], Lars Kasper[2,3], Maria Engel[2], Jennifer Nussbaum[2], Bertram J. Wilm[2,4], Klaas P Pruessmann[2], S. Johanna Vannesjo[1]

[1)] *Wellcome Centre for Integrative Neuroimaging, FMRIB, Nuffield Department of Clinical Neurosciences, University of Oxford, Oxford, United Kingdom*

[2)] *Institute for Biomedical Engineering, University and ETH Zurich, Zurich, Switzerland*

[3)] *Translational Neuromodeling Unit, Institute for Biomedical Engineering, University of Zurich and ETH Zurich, Zurich, Switzerland*

[4)] *Skope Magnetic Resonance Technologies, Zurich, Switzerland*

**Key words:**

Functional MRI, fMRI, Spirals, LTI, Gradient Impulse Response Function, GIRF

**Corresponding author:**
S. Johanna Vannesjo
johanna.vannesjo@gmail.com

# Highlights

- This work investigates the feasibility of using a one-time system calibration (called GIRF) based on a linear time-invariant gradient model to account for k-space trajectory deviations in spiral fMRI.
- We show that the image quality and the spatial specificity of the fMRI activation are substantially improved when using the GIRF-prediction for trajectory correction while the nominal reconstructions suffer from artifacts and mis-placed fMRI activation.
- We demonstrate that system characterization via the GIRF can enable spiral fMRI in situations when concurrent monitoring is not available.

# Abstract

**Purpose:** Spiral imaging is very well suited for functional MRI, however its use has been limited by the fact that artifacts caused by gradient imperfections and $B_0$ inhomogeneity are more difficult to correct compared to EPI and requires accurate knowledge of the traversed k-space trajectory. With the goal of making spiral fMRI more accessible we have evaluated image reconstruction using trajectories predicted by the gradient impulse response function (GIRF), which can be determined in a one-time calibration step.

**Methods:** GIRF-predicted reconstruction was tested for high-resolution (0.8mm) fMRI at 7T. Image quality and functional results of the reconstructions using GIRF-prediction were compared to reconstructions using the delay corrected nominal trajectory and concurrent field monitoring.

**Results:** The reconstructions using nominal spiral trajectories contain substantial artifacts and activation maps contain mis-placed activation. Image artifacts are substantially reduced when using the GIRF-predicted reconstruction and the activation maps for the GIRF-predicted and monitored reconstructions largely overlap. The GIRF reconstruction provides a large increase in the spatial specificity of the activation compared to the nominal reconstruction.

**Conclusion:** The GIRF-reconstruction generates image quality and fMRI results similar to using a concurrently monitored trajectory. The presented approach does not prolong or complicate the fMRI acquisition. Using GIRF-predicted trajectories has the potential to enable high-quality high-resolution fMRI in situations where concurrent monitoring is not available.

# Introduction

Blood Oxygen Level Dependent (BOLD) functional magnetic resonance imaging (fMRI) requires fast imaging for which the current gold standard are acquisitions with an Echo Planar Imaging (EPI) readout. Spiral readouts have many desirable properties for rapid acquisitions and have long been considered a promising alternative to EPI for fMRI (Glover, 2012): They can provide higher k-space sampling efficiency compared to EPI sampling (Glover, 2012; Glover and A. T. Lee, 1995; Noll et al., 1995) and allow a more flexible choice of echo time (TE). The latter is especially useful for high-resolution fMRI at 7T or above where for EPI large parallel imaging factors or Partial Fourier are required to achieve the optimal TE for BOLD contrast. Further, spiral-in/out trajectories (Glover and Law, 2001) can increase the acquisition efficiency and can improve fMRI in regions prone to dropout, such as the orbitofrontal cortex. Finally, spiral imaging naturally has reduced sensitivity to pulsatile motion (Glover and A. T. Lee, 1995; Yang et al., 1998) and under-sampled non-Cartesian imaging results in relatively incoherent aliasing, which is less detrimental to image quality compared to coherent aliasing, which occurs in under-sampled EPI (Wright et al., 2014).

Despite these advantages spiral imaging has not yet become a mainstream fMRI acquisition strategy. The reasons for the slow uptake of spiral fMRI include the fact that artifacts caused by gradient imperfections (discrepancy between the actual and nominal gradients) and $B_0$ inhomogeneities are more difficult to correct for spiral trajectories compared to EPI. Localized off-resonance resulting from susceptibility-induced field inhomogeneities cause dropout and shifts in EPI for which a number of established correction methods exist (Andersson et al., 2003; Smith et al., 2004). Similarly for gradient infidelity, the correction of the Nyquist ghost artifact in EPI is considered a routine step in image reconstruction, for example using navigator lines acquired before the readout (Schmitt et al., 1998). For spiral readouts, $B_0$ inhomogeneities and trajectory imperfections cause blurring and geometric distortions. To reduce these issues gradient delay correction is typically performed in spiral imaging (Börnert et al., 1999). However this is usually not as effective as the EPI delay correction, and spiral fMRI images have often been blurry as a result, especially around the air-tissue interfaces in the frontal sinuses and ear canals.

Monitoring of the encoding fields during the acquisition using Nuclear Magnetic Resonance

(NMR) field probes (Barmet et al., 2008; De Zanche et al., 2008) allows for precise measurement of the traversed k-space trajectory. In conjunction with a $B_0$ field map covering the imaging FOV, included in a model-based reconstruction, this yields high-quality spiral imaging (Engel et al., 2018; Kasper et al., 2018; Wilm et al., 2016). This has been shown to enable high-resolution spiral fMRI (Kasper et al., 2017; Kasper et al., 2019). However, the required setup for concurrent monitoring might not always be available, in which case modeling the behavior of the gradient chain can be an alternative.

Deviations from the prescribed encoding which are reproducible (for example, induced by eddy currents) can be corrected by using a model to characterize the gradients. It has been shown (Addy et al., 2012; Vannesjo et al., 2013) that to a high degree of accuracy the gradient chain can be considered as a linear, time invariant (LTI) system. For an LTI system, the relation between the input to the system and its output is determined by the impulse response of the system – in the case of the gradient chain, the gradient impulse response function (GIRF).

We have previously shown for a range of different trajectories that GIRF-prediction enables high quality image reconstruction with only minor image quality differences to using the monitored trajectory (Vannesjo et al., 2016). This evaluation was performed on individual images. In fMRI, however, we perform high duty cycle imaging over extended periods of time (5-10 minutes for a typical fMRI run with a single fMRI session often containing multiple runs). We know that gradient heating over the course of an fMRI experiment violates the LTI assumption at the basis of the GIRF prediction. But we do not know to what extent this will affect an image time-series, such as required for fMRI. The aim of the present work is to evaluate the utility of GIRF-based reconstruction for functional MRI. The results are assessed by comparison with reconstructions based on concurrent field monitoring and nominal trajectories with optimal delay correction.

# Methods

All data were acquired on a 7T Achieva system (Philips Healthcare, Best, Netherlands) using a quadrature-transmit coil and 32-channel head receive array (Nova Medical, Wilmington, MA). The manufacturer's built-in eddy current compensation was kept activated for all experiments.

### GIRF measurement and GIRF-based trajectory prediction

If a system is linear and time-invariant it can be described via its impulse response function, which is the output of the system to a very brief input pulse. Knowledge of the system's impulse response allows predicting the system response *o(t)* via convolution of the input waveform *i(t)* with the impulse response (equation [1]). In the frequency domain this corresponds to a multiplication with the Fourier transform of the impulse response [2] (typically called the system transfer function – for simplicity we use the acronym *GIRF* referring to the gradient response function both in the time and in the frequency domain).

$$o(t) = \int i(\tau) \cdot girf(t-\tau) \cdot d\tau \qquad [1]$$

$$O(\omega) = I(\omega) \cdot GIRF(\omega) \qquad [2]$$

The characterization of the 7T scanners gradient chain was performed similarly as described by Vannesjo et al. (Vannesjo et al., 2013): A set of gradient input pulses were played out and the resulting magnetic fields were measured with a dynamic field camera (Dietrich et al., 2016) consisting of 16 $^{1}$H NMR field probes distributed on the surface of a sphere of 10 cm radius. This allows fitting of spherical harmonic basis functions up to 3$^{rd}$ order to the probe measurements. The GIRF was calculated via frequency-domain division of the measured output by the known inputs (using least-squares combination of data from different input pulses). For an accurate GIRF calibration the input gradient pulses should cover the entire range of expected frequencies, while complying with hardware and acquisition time constraints. This was achieved by using 12 different triangular pulses (slew rate 200 T/m/s, time-to-peak 20–158 ms at ~12-ms increments). The GIRF measurements took approximately 3 minutes (12 gradient pulses, 3 gradient directions, 4 averages, 1.2 s TR). The individual probe signals were corrected for concomitant fields terms which are a known deviation from the LTI assumption (for details see (Vannesjo et al., 2016)). This correction was also applied to the concurrent field monitoring data described in the next section.

GIRF-based gradient time courses were determined via frequency-domain multiplication of the nominal gradient time course with the measured GIRFs.

**Concurrent field monitoring**

Concurrent field monitoring was performed during all scans using NMR field probes clip-

mounted (Barmet et al., 2008) on the 32-channel head receive coil. The probe data was fitted to up to 1$^{st}$ order spherical harmonics producing linear gradient field terms in the three orthogonal directions (and the corresponding k-space trajectory $k_x$,$k_y$,$k_z$), as well as a 0$^{th}$-order field term ($k_0$), which reflects global field changes over time.

The field probes were excited before the readout gradient starts and were read out concurrently with the head-coil acquisition. Due to the long readout and the strong gradients applied the probe signal can de-phase prior to the end of the monitoring period. Each probe's signal was therefore visually inspected and if the probe signal had very low amplitude and the signal phase exhibited discontinuities the probe was excluded from the spherical harmonic fit. Per subject between 5-7 probes (on average 6.2) were excluded in this study, leaving approximately 10 probes.

Undesired saturation of the NMR field probe signal can occur if the repetition time of the probe excitation is short relative to the $T_1$ of the probes. To allow sufficient signal recovery between measurements the field camera recording was performed on every third slice. For the non-monitored slices the k-space trajectory from the last monitored slice was used.

**FMRI acquisition**

The data collected in this work was also used in a recent publication exploring the use of concurrently monitored single-shot spirals for fMRI (Kasper et al., 2019). Data were collected from seven healthy volunteers in accordance with the local ethics regulations. The visual fMRI paradigm used a simple retinotopic mapping (Warnking et al., 2002) protocol, designed to stimulate quarter-fields of the visual cortex, similar to the one used in (Kasper et al., 2014). The subjects were presented with 15 s blocks of two flickering, color-changing 90° wedges separated by 180° interleaved with 15 s of rest (fixation cross). Alternating blocks of upper left/lower right (ULLR) and blocks of upper right/lower left (URLL) wedges were presented over 100 volumes (~330s). The subjects were instructed to fixate on a point at the center between the wedges. In order to maintain the subjects' attention, they were asked to respond to any contrast alteration of the fixation point via button box.

We used a multi-slice 2D gradient-echo sequence with a single-shot Archimedean spiral-out

readout (designed according to (Lustig et al., 2008)) of 59 ms duration. The radial spacing of samples was chosen to under-sample k-space by a factor of 4 with respect to the field-of-view (FOV) of 23 cm. The transversal images were acquired with an in-plane resolution of 0.8 mm isotropic and a TE of 25 ms, selected for optimal BOLD contrast. 36 slices of 0.89 mm thickness (with a slice gap of 0.11 mm) were acquired, resulting in a FOV of 23x23x3.6 cm and a volume TR of 3.3 s. Excitations were preceded by a Spectral Presaturation with Inversion Recovery (SPIR) fat suppression module.

A Cartesian multi-echo GRE scan (FOV = 23 cm, resolution = 1 mm isotropic, $TE_1$=4ms, $\Delta TE$ = 1ms, 6 echoes collected) was collected to estimate coil sensitivities and $B_0$ maps. The $B_0$ maps were calculated by voxel-vise fitting the signal phase over the different echoes. The coil sensitivities were estimated from the first echo of this data.

One subject was excluded from the study due to subject motion. The data from the six remaining volunteers were reconstructed and analyzed as described below.

**Image reconstruction and processing**

The images were reconstructed offline in Matlab using CG-SENSE (Pruessmann et al., 2001) with multi-frequency interpolation for fast off-resonance correction (Sutton et al., 2003). For each data set three reconstructions were performed using the following k-space trajectories:

1. Delay-corrected nominal trajectory (labeled *nominal* in figures)
2. GIRF-predicted trajectory (labeled *GIRF* or *GIRF-predicted* in figures)
3. trajectory measured with concurrent field monitoring (labeled *monitored* in figures).

For the monitored and GIRF-predicted reconstructions the imaging data was demodulated by the measured/predicted $0^{th}$-order field integrals $k_0$.

A center frequency adjustment is a typical fMRI pre-scan, which was not performed in this study because it is redundant when using concurrent field monitoring. In order to not artificially disadvantage the GIRF-predicted and nominal reconstructions we performed a processing step equivalent to frequency adjustment. The center frequency was determined via a linear fit on the

first 0.9 ms of the monitored $k_0$ (first slice of the first volume, before the readout gradient starts). The imaging data was then demodulated by the center frequency for the nominal and the GIRF-predicted reconstruction.

The nominal trajectories were delay-corrected prior to reconstruction. We minimized the RMSE trajectory difference between the nominal and the monitored trajectory on the first readout of the time series. A global delay was chosen for the x and y gradient axes as the small differences between the two axes were within the standard deviation of the delay calibration).

The reconstructed image time series was corrected for subject translations and rotations (McFLIRT/FSL). The data was pre-whitened (FILM/FSL) and GLM-analysis was performed using FEAT in FSL(Jenkinson et al., 2012). Activation was assessed using z-statistics contrasting ULLR versus URLL. In order to produce fMRI data with high spatial specificity we performed no spatial smoothing or clustering.

All of the analysis was performed on a per-subject basis in the space of each subject's functional data to avoid any degradation of the spatial resolution by registration. The first echo of the multi-echo GRE was used as the subjects' structural scans. For the analysis of the functional results, masks of the grey matter and white matter in the visual cortex were determined as an intersection of a V1-V3 mask (using Juelich atlas (Eickhoff et al., 2005; Zilles and Amunts, 2010) labels 81-86 in FSL) and subject-specific GM/WM masks generated by segmenting the structural image using FAST/FSL (Zhang et al., 2001). A significance threshold of $z > 2.3$ ($p < 0.01$) was used for all the activation maps shown. In table 1 the average and $90^{th}$ percentile of the absolute value of significant z-stats within the GM V1-V3 ROI are reported.

The concurrently monitored trajectories and the resulting image reconstructions were used as reference to assess the nominal and GIRF-predicted data. For example, in table 1 the trajectory error and image artifacts are quantified as root-mean-squared error (RMSE) compared to concurrent monitoring, and figure 6 shows how much the GIRF/nominal z-statistic maps deviate compared to the measured one. Receiver operator characteristic (ROC) curves were used to additionally provide a comparison of the fMRI results without selecting the monitored reconstruction as the ground truth. ROC analysis typically involves plotting the number of true-positive activations against the number of false-positive findings. In this work we used the

subject-specific gray and white matter masks of V1-V3 to identify “true positives” and “false positives” respectively and plotted this while varying the z-statistic threshold from 0 to the maximum z present in the data. The area under the curve (AUC) gives a measure of spatial specificity and was used to compare between the reconstructions. In addition to not requiring a ground truth, this analysis has the advantage of not depending on a specific significance threshold (for example $z > 2.3$).

The temporal SNR (tSNR) was evaluated in the motion-corrected fMRI time series, and was calculated on a voxel-by-voxel basis as the mean signal over time divided by the temporal standard deviation of the signal. The tSNR was averaged over the GM V1-V3 ROI and reported in table 1 for each subject and reconstruction.

# Results

The delay-corrected nominal spiral trajectory deviates substantially from the one measured with the NMR field probes, especially close to the center of k-space where the gradients are rapidly changing (Fig.1 a-c). For the example subject shown in Fig. 1 the distance between the nominal and the measured trajectory reach ~1.5*1/FOV. The GIRF-predicted spiral trajectories follow the measured ones much more closely until about 40 ms into the spiral readout. Towards the edge of k-space however there is little improvement from the GIRF-predicted trajectories over the nominal ones (for the example subject in Fig. 1 the maximum k-space deviation between the GIRF-predicted and the nominal trajectories is ~0.75*1/FOV).

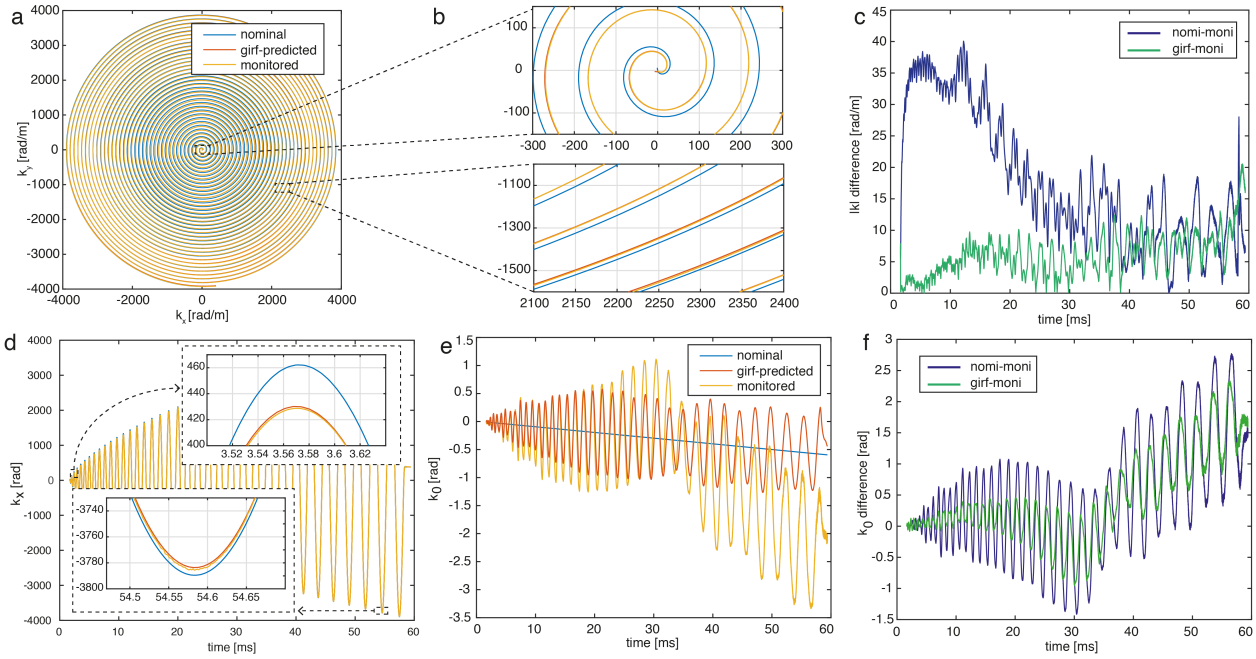


Figure 1: Comparison of a nominal delay-corrected, GIRF-predicted and concurrently monitored spiral trajectory. (a) An example spiral trajectory and (b) zooms highlighting differences between the three trajectories. (c) The k-space distance between nominal/GIRF-predicted and monitored is shown to quantify differences over the course of one spiral readout. (d) Spiral readout (x-axis) including zooms. (e) The zero order field term $k_0$ over one readout. Note that the nominal $k_0$ has a non-zero slope due to the retrospective "frequency adjustment" correction applied. (f) Difference of nominal/GIRF-predicted to measured $k_0$.

The root-mean-square trajectory error (RMSE), defined here as the Euclidian distance to the monitored trajectory, averaged for all slices and volumes, is reported for all subjects in table 1. Averaged over all subjects the nominal RMSE and GIRF-predicted RMSE were 19.66 rad/m and 10.85 rad/m respectively. This corresponds to a ~45% RMSE reduction when using GIRF prediction over nominal trajectories. Figure 1d/e shows the concurrently monitored, GIRF-predicted and nominal $k_0$. The zero-order phase offset $k_0$ reflects global variations in $B_0$. Demodulation with an accurate estimate of $k_0$ can substantially improve image quality (Vannesjo et al., 2016). The measured $k_0$ oscillations are closely coupled with those of the spiral readout gradients. This is partially predicted by the GIRF but the amplitude of oscillations is not captured accurately. Additionally, the $k_0$ exhibits slower trends over the readout, for example a change in slope at about 35 ms, which are not captured by the GIRF. These slower dynamics are qualitatively similar across subjects but are not captured by the GIRF prediction, suggesting that they are not linearly related to the gradient waveform. Average RMSE over all subjects (see table 1 for results for individual subjects) is 1.06 rad for nominal $k_0$ and 0.94 rad for GIRF-predicted $k_0$, which corresponds to an improvement of 11%.

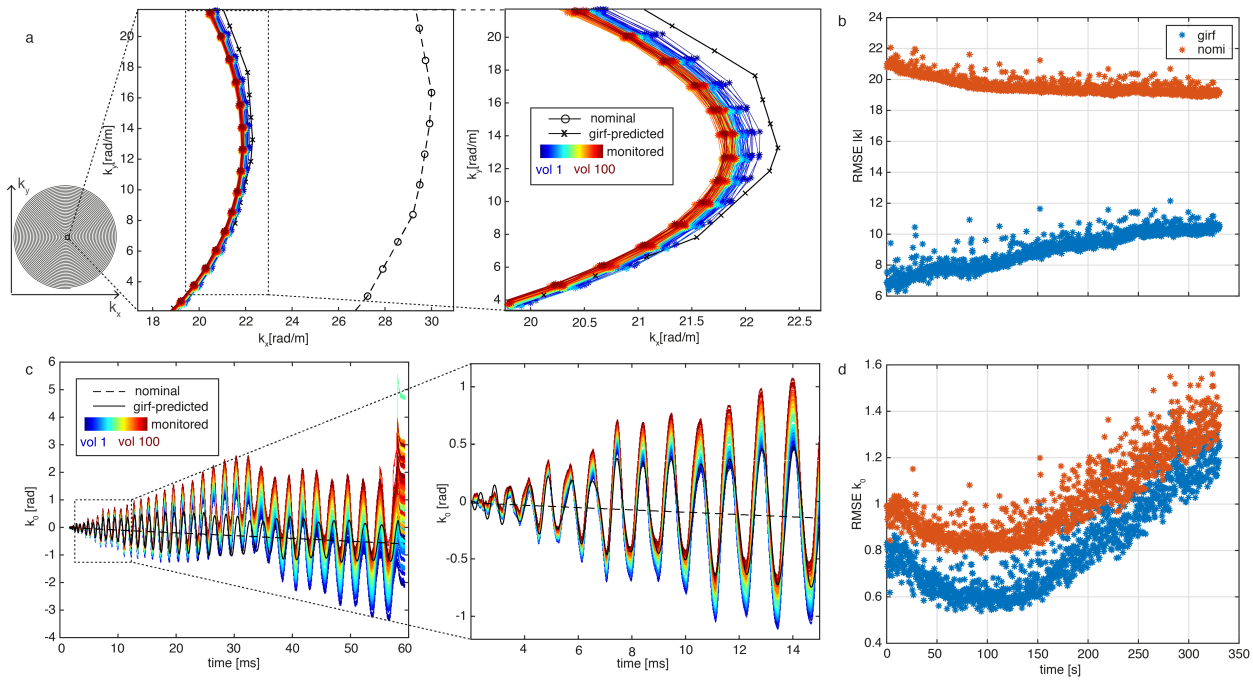


Figure 2: Evolution of k-space trajectories over the fMRI experiment showing how (a) monitored spiral trajectory changes form the first volume (dark blue) to the last (dark red) including zoom and (b) RMSE on the k-space distance, |k|, for the nominal/GIRF-predicted trajectories with respect to the monitored one. In the lower row (c) $k_0$ with zoom and (d) RMSE of the nominal/GIRF-predicted $k_0$ with respect to the measured one are shown.

The GIRF-predicted and nominal trajectories are the same for all reconstructions whereas the monitored trajectory is updated every 3rd readout. Fig. 2 illustrates how much the trajectory changes over the course of the fMRI experiment. Over the 5.5 minute experiment the trajectory gradually shifts from the first volume (blue) to the last volume (red), likely due to gradient heating.

| | Subjects → | 1 | 2 | 3 | 4 | 5 | 6 | Mean |
|---|---|---|---|---|---|---|---|---|
| Trajectories | RMSE \|k\| nomi | 19.78 | 19.60 | 20.84 | 19.63 | 18.67 | 19.40 | 19.66 |
| | RMSE \|k\| GIRF | 9.85 | 10.66 | 12.80 | 9.07 | 10.55 | 12.19 | 10.85 |
| | RMSE $k_0$ nomi | 1.186 | 0.89 | 1.078 | 1.04 | 1.34 | 0.85 | 1.06 |
| | RMSE $k_0$ GIRF | 1.11 | 0.75 | 0.90 | 0.84 | 1.24 | 0.81 | 0.94 |
| Images | RMSE nomi | 6.34 | 6.45 | 5.22 | 6.97 | 5.03 | 5.06 | 5.85 |
| | RMSE GIRF | 2.01 | 2.07 | 1.98 | 2.36 | 2.52 | 1.95 | 2.15 |
| tSNR | tSNR moni | 16.44 | 19.39 | 14.98 | 15.43 | 13.95 | 15.4 | 15.93 |
| | tSNR GIRF | 14.94 | 18.25 | 14.23 | 14.71 | 13.37 | 14.7 | 15.03 |
| | tSNR nomi | 15.47 | 19.42 | 14.90 | 15.66 | 14.09 | 15.5 | 15.84 |
| fMRI | mean zstat moni | 3.74 | 4.09 | 3.98 | 4.33 | 4.04 | 3.72 | 3.98 |
| | mean zstat GIRF | 3.66 | 3.92 | 3.86 | 4.14 | 3.73 | 3.75 | 3.84 |
| | mean zstat nomi | 3.54 | 3.94 | 3.85 | 3.84 | 3.55 | 3.81 | 3.76 |
| | 90th perct. moni | 5.72 | 6.74 | 6.34 | 7.13 | 6.62 | 5.76 | 6.39 |
| | 90th perct. GIRF | 5.58 | 6.35 | 6.04 | 6.74 | 5.77 | 5.88 | 6.06 |
| | 90th perct. nomi | 5.14 | 6.20 | 5.83 | 5.97 | 5.32 | 5.94 | 5.73 |
| | ROC AUC moni | 928 | 758 | 860 | 1062 | 624 | 755 | 831 |

| | | | | | | | | |
|---|---|---|---|---|---|---|---|---|
| | ROC AUC GIRF | 809 | 615 | 703 | 981 | 577 | 723 | 735 |
| | ROC AUC nomi | 548 | 341 | 266 | 295 | 80 | 463 | 332 |

Table 1: Results summary metrics for all subjects (from top to bottom): RMSE trajectory errors for the k-space distance, |k|, and the zero order field term, $k_0$, using the monitored trajectory as the ground truth, RMSE image error using the monitored reconstruction as the reference, average tSNR in the brain, average and $90^{th}$ percentile z-statistics in the GM V1-V3 ROI and the AUC from the ROC plots to evaluate spatial specificity of the z-statistic maps.

The nominal spiral images are corrupted by blurring and geometric distortion (Fig 3). The GIRF-predicted reconstruction provides improved image quality. Residual artifacts (mainly subtle blurring and some ringing) can be observed in the difference images to the monitored reconstruction. The global image artifact levels, defined here as the RMSE to the monitored reconstruction averaged over all voxels in a brain mask and all volumes in the fMRI time-series, are reported in table 1. Averaged over all subjects the artifact level was 5.85 for nominal image reconstructions and 2.15 for GIRF-predicted $k_0$, which corresponds to an improvement of 63%.

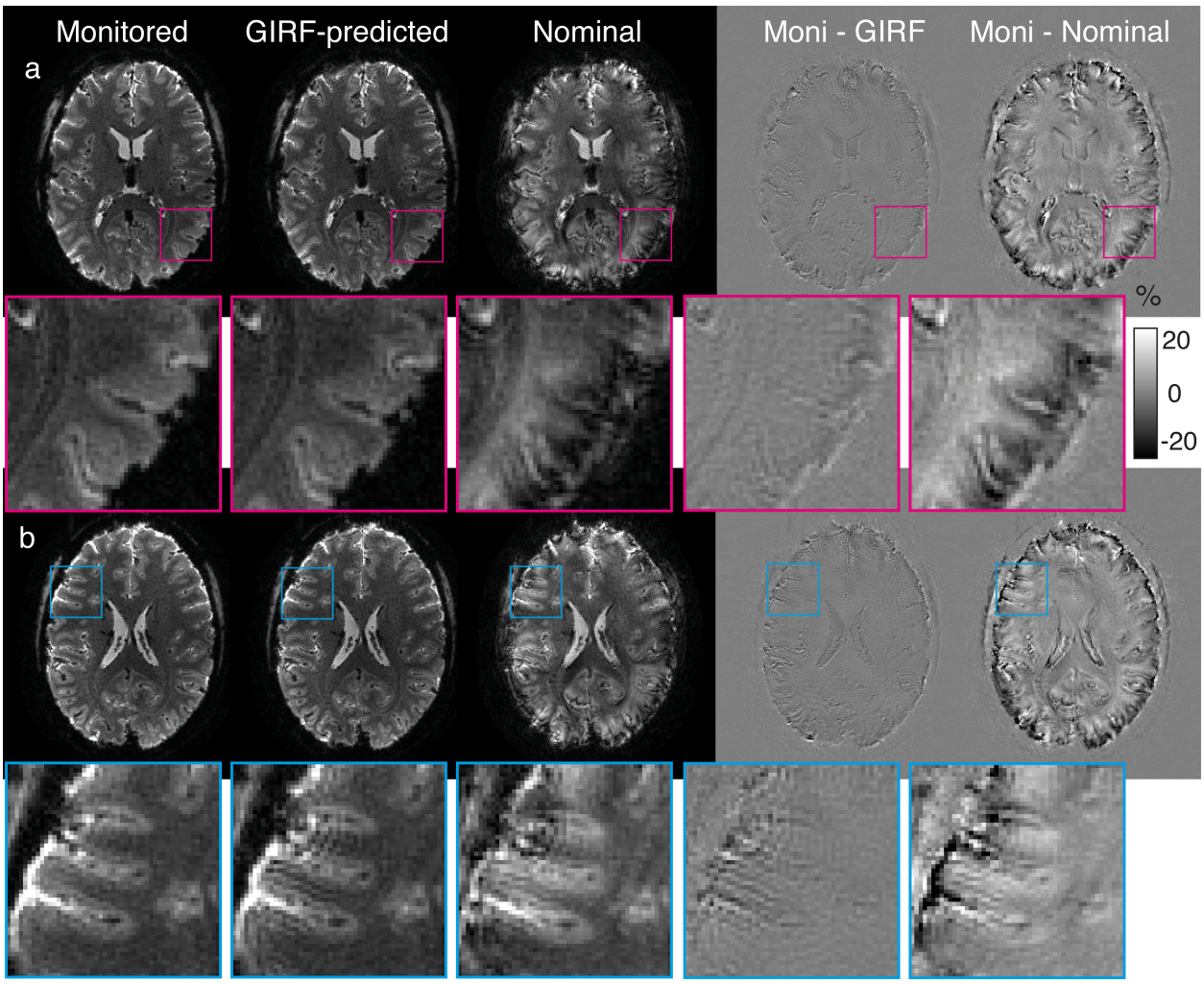


Figure 3: Image quality comparison of reconstructions using monitored trajectories (left), GIRF-predicted trajectories (centre) and nominal trajectories (right) for two difference slices for an example subject. To the right of each sub-figure, the differences to the corresponding reconstructions based on the monitored trajectory are displayed. The difference images are scaled to percent of the maximum value in the monitored reconstruction. In the inferior slice (a) the GIRF-predicted recon only contains a small increase in blurring compared to the monitored reconstruction. In a superior example slice (b) the GIRF-predicted recon additionally exhibits an increase in ringing artifacts.

A comparison of the first and final volume in the fMRI time series revealed an increase in image artifacts over time for the GIRF reconstruction (shown for an example subject in Fig. 4). However, the image artifact reduction compared to nominal still corresponds to 57% in the final volume compared to 65% for the first volume (averaged over all subjects).

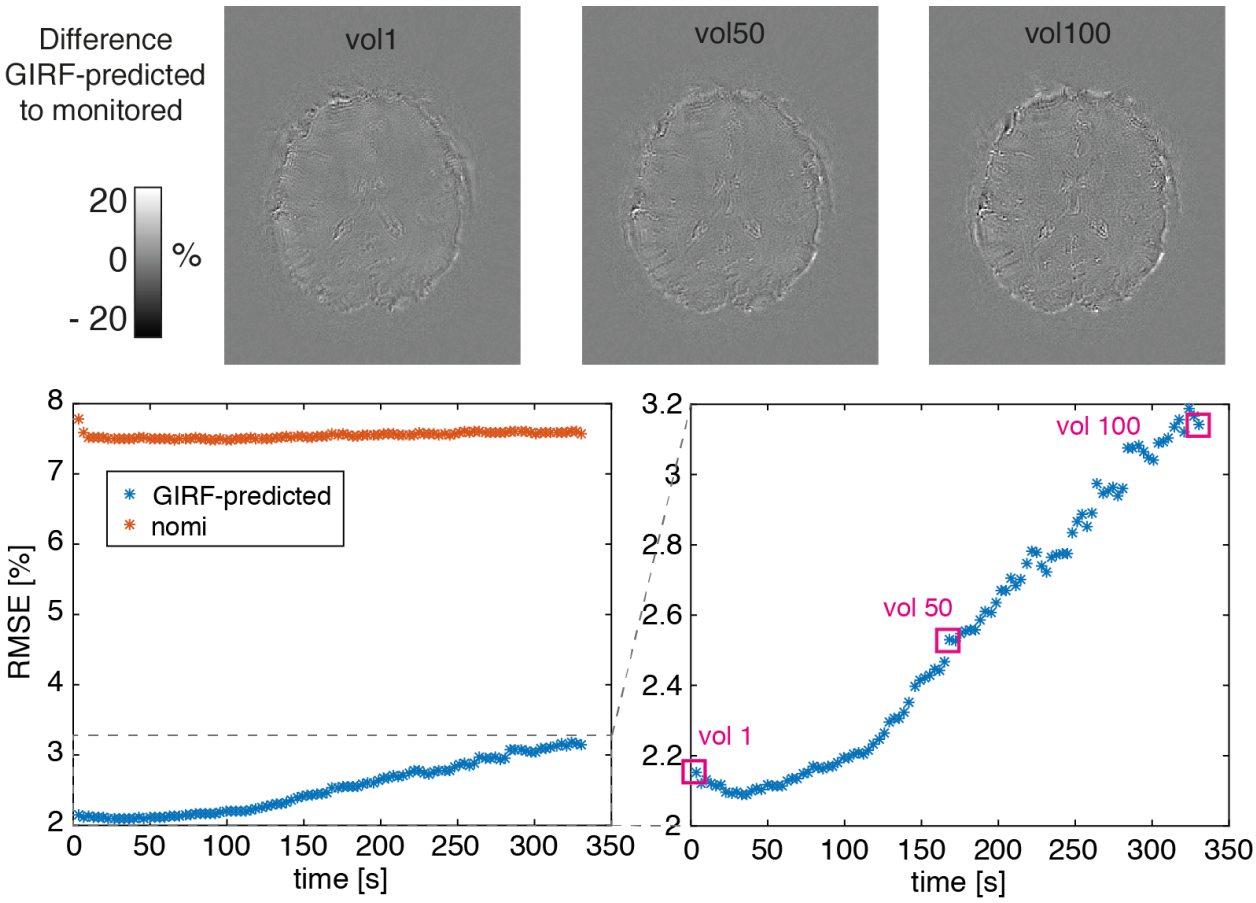


Figure 4: Quality of GIRF-predicted reconstruction over fMRI time-series: Top row shows difference images of monitored and GIRF-predicted reconstructions at the start, middle and the end of the 330-second fMRI acquisition. The bottom row shows the RMSE for GIRF-predicted/nominal reconstructions with respect to the monitored one. A zoom showing the dynamics of the GIRF-predicted RMSE is shown on the bottom right.

The average temporal SNR over all subjects (table 1) is highest for monitored reconstructions, slightly lower for the nominal recon (<1% reduction) and lowest for the reconstructions using GIRF-predicted trajectories (~5% reduction). We expect the reconstructions using concurrent monitoring to have slightly improved tSNR as we are reducing the temporal variance by correcting for field effects caused by long-term gradient heating and physiological field fluctuations. This is not captured by the GIRF where we use the same trajectory for each volume. The higher tSNR of the nominal reconstruction could potentially be explained by the larger amount of blurring present, which acts as a local averaging kernel.

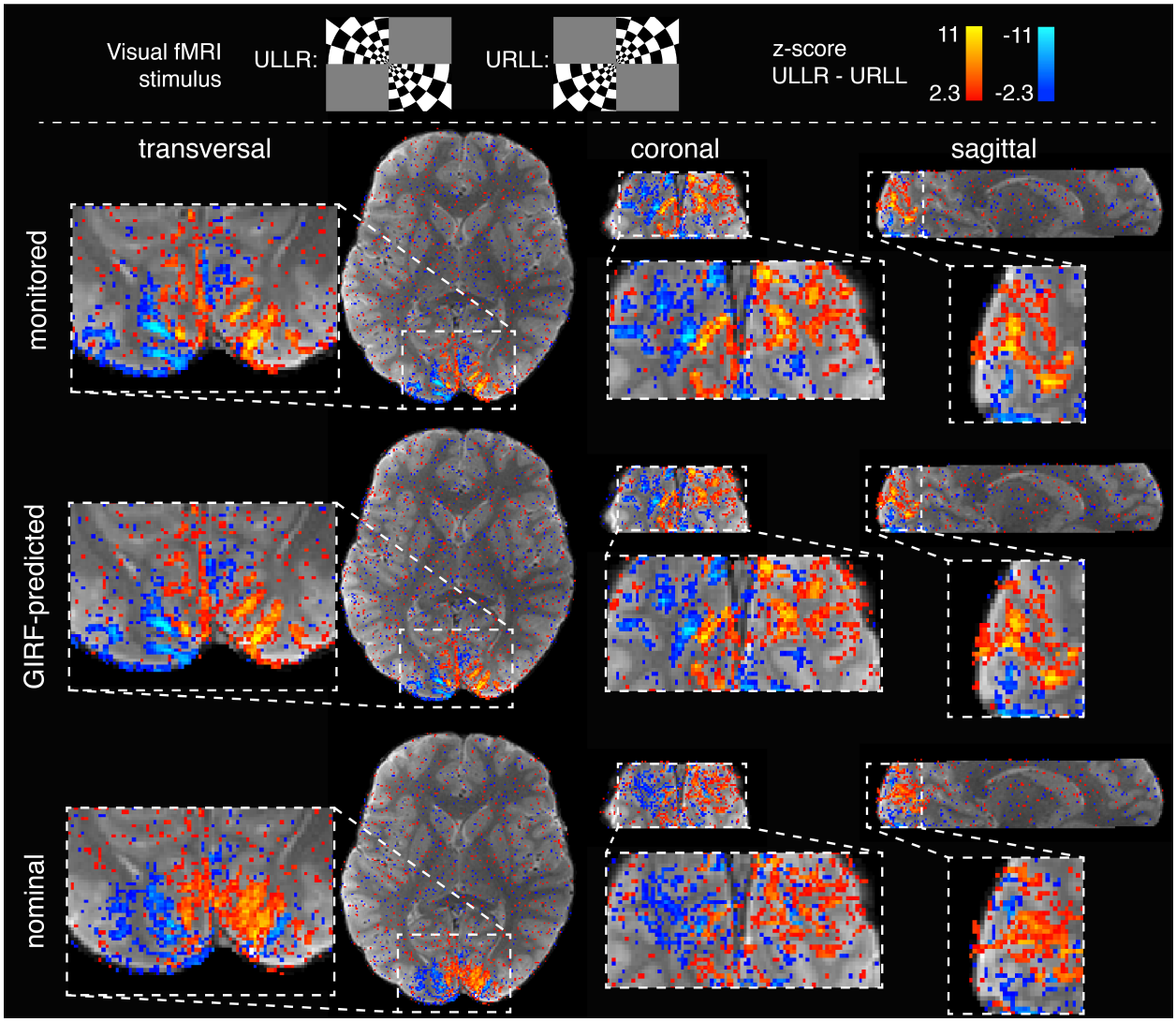


Figure 5: Evaluation of the fMRI experiment designed to stimulate the quarter-fields of the visual cortex. Z-statistic maps (contrasting ULLR versus URLL) overlaid on the subject's structural image. The activation for the monitored and GIRF-predicted reconstructions match the grey matter architecture well, as seen for example along the calcarine sulcus (sagittal view), while the nominal reconstruction results in misplaced activation.

For the monitored and GIRF-predicted reconstructions, the spiral fMRI results show good correspondence of the activation with gray matter architecture (Figs. 5-6), while the nominal data contain misplaced activation (apparent for example where activation is crossing white matter boundaries). The activation maps for the GIRF-predicted and monitored reconstructions overlap largely (Fig. 6).

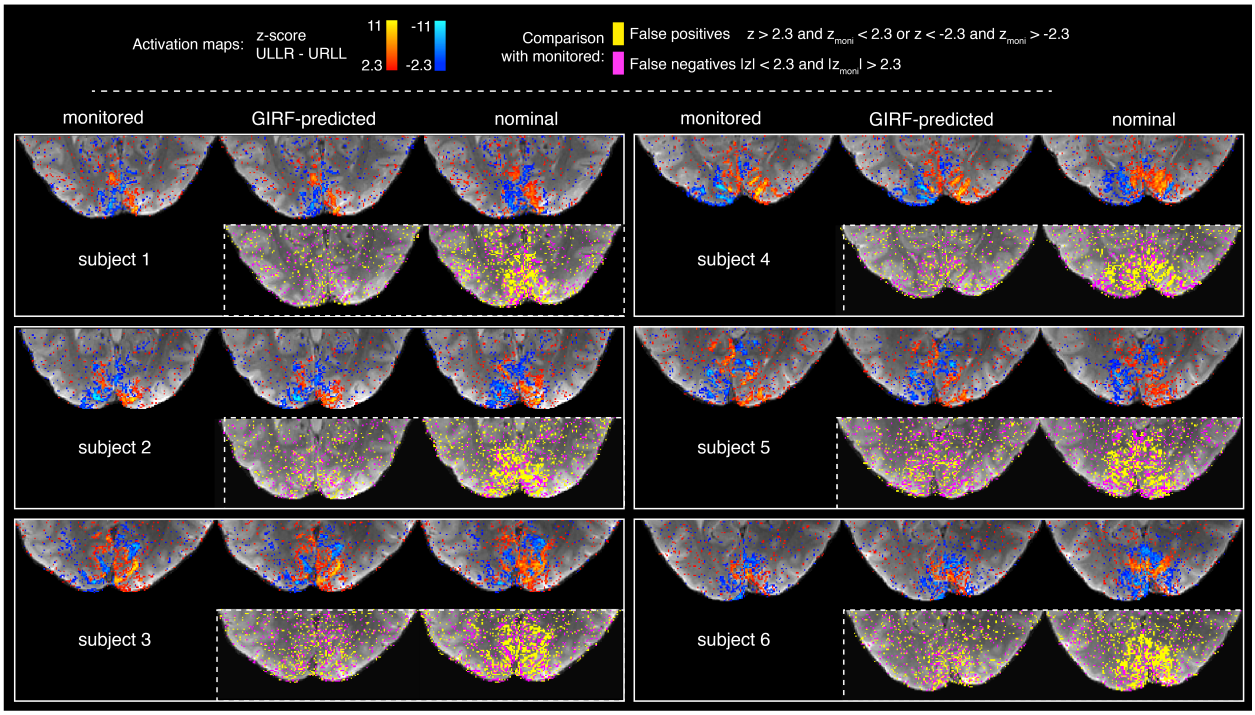


Figure 6: Activation maps (transversal section of visual cortex) for six subjects. Maps of false positives (yellow) and false negatives (pink) with respect to the monitored reconstruction are displayed below each GIRF-predicted and nominal image.

The increased specificity for the GIRF-predicted reconstructions is confirmed by the ROC analysis (Fig. 7). The GIRF reconstruction provides a large increase in specificity, compared to the nominal reconstruction (~122% increase in specificity as captured by the AUC, averaged over all subjects). The monitored reconstruction in turn provides a smaller additional improvement over the GIRF reconstructed z-stats (average increase of ~13%). The ROC analysis assumes that all activated voxels within the GM V1-V3 ROI are true positives. Note that this is different to how true positives are defined in the z-statistics map comparison with monitored as the ground truth.

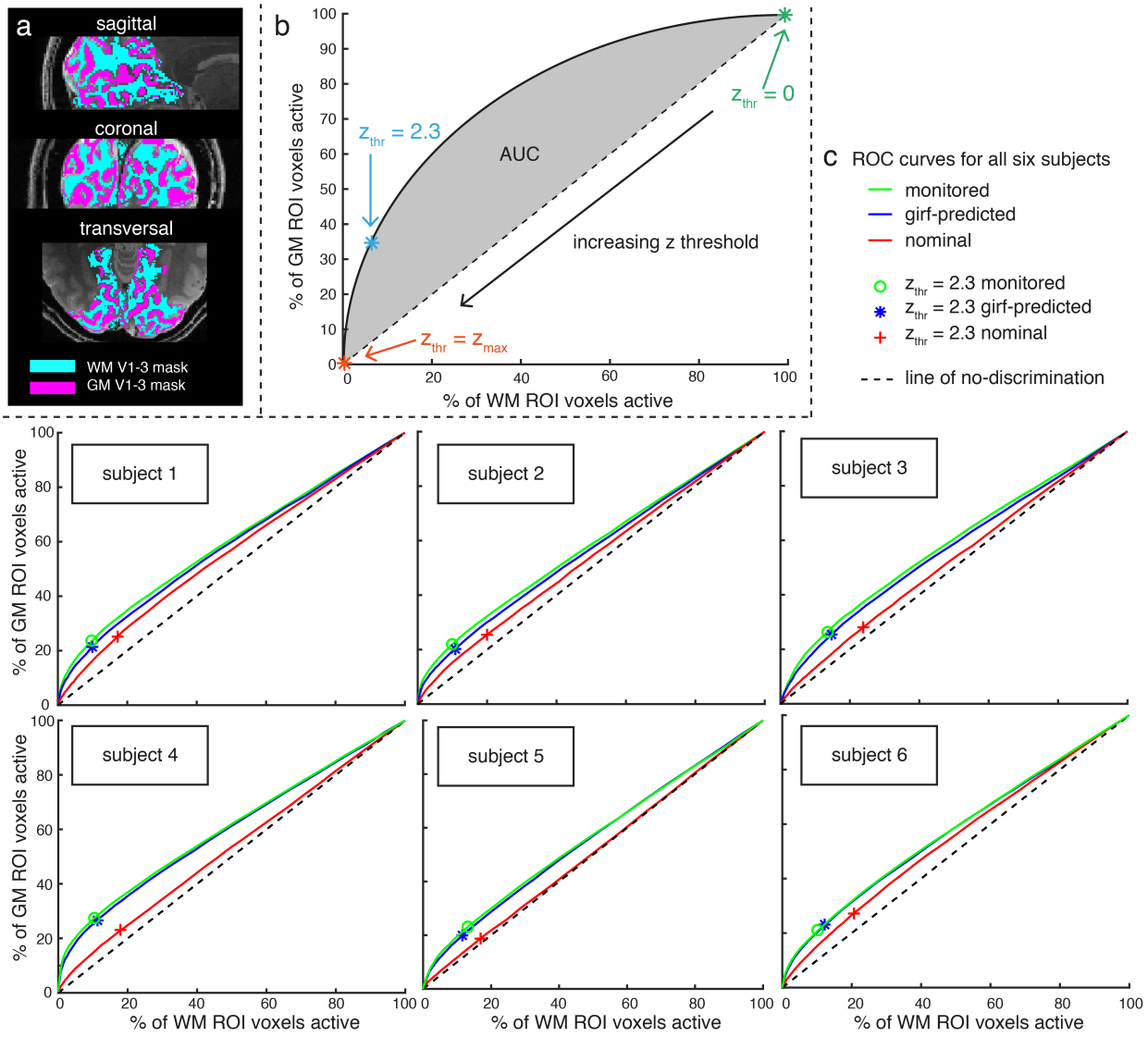


Figure 7: (a) Grey and white matter masks of V1-V3 used for the analysis. (b) Schematic explaining receiver operating characteristic (ROC) curve analysis used to assess the spatial specificity of the different reconstructions (without having to choose a specific one as ground truth). The dashed line is the line of no discrimination, indicating equal amounts of true and false positives. The area under the curves (AUC) values were used as a summary metric and are reported in table 1. (c) ROC curves for all six subjects, indicating that the spatial specificity of the activation is highest for the monitored reconstructions. The GIRF-predicted reconstruction results in only slightly reduced specificity whereas the nominal curve lies substantially closer to the line of no discrimination.

# Discussion

The results presented above show that the reconstructions using the nominal trajectory contain a large amount of artifacts (blurring, ringing and distortion) while the monitored and GIRF-predicted trajectories enable high-quality image reconstruction. The main goal of this work was

to determine if image reconstruction using GIRF-predicted trajectories is suitable for use in functional MRI where long high-duty cycle acquisitions cause heating of the gradient coils and the surrounding structures. The temperature increase alters electrical and mechanical material properties and thus changes the behavior of the gradient chain. This is a deviation from the LTI assumption underlying the GIRF approach. We observed an increase in artifacts in the GIRF-predicted reconstructions over the course of the fMRI acquisition. This is expected as the GIRF measurement (which is relatively low duty cycle itself) was performed starting "from cold" (no high duty-cycle scanning run beforehand). Therefore, towards the end of an fMRI time series the gradients are in a different thermal state to the one they were characterized in. Overall the impact of this on the fMRI results is small. The spatial specificity of the GIRF-predicted fMRI results is very close to the monitored ones while it is substantially reduced for the nominal reconstruction. In the z-statistic maps from the nominal reconstruction we see mis-placed activation, which is not localized to the gray matter due to the blurring and other artifacts present in the image.

The delay correction of the nominal trajectory did not improve the image quality much (over not performing delay correction), which stands in contrast to EPI where calibrating a delay between odd and even lines typically allows substantial artifact reduction. The spiral readout gradients sweep a large range of temporal frequencies, whereas the EPI has a dominant peak at the switching frequency. Presumably for this reason, a single delay works well in EPI compared to spirals where it is important to know the full response over a large range of frequencies.

$B_0$ related artifacts dropout and distortion scale with field strength, therefore it is especially important to include $B_0$ correction for fMRI at 7T. For the nominal reconstructions the artifacts are worst near the air-tissue interfaces where $B_0$ inhomogeneity is large despite the fact that static $B_0$ is accounted for in all reconstructions. This is because $B_0$ correction relies on geometric congruency between the field map and the encoded image (Spirig et al. 2017). Accurate knowledge of the encoding fields therefore becomes even more important at ultra-high field.

We further evaluated the spatial specificity of the GIRF-predicted reconstruction, to test suitability of the approach for high-resolution fMRI, as for example required to detect activation on the level of cortical lamina and columns. We assessed the spatial specificity using a ROC-style analysis, which allows quantifying specificity without choosing one reconstruction as a

ground truth and is independent of a specific significance threshold. The challenge with this method is that it requires accurate true/false positive masks, which relies on accurate segmentation and registration of an anatomical atlas to the subjects' functional data.

The GIRF-predicted trajectories consistently provided good results for all subjects acquired. There were some inter-subject differences in how closely the GIRF-predicted reconstructions match the monitored ones (see Fig. 5 and 7). The fMRI scans used in this study were acquired at different time points within the scanning session (sometimes it was the first longer scan of the session whereas other times a few other fMRI runs had been performed immediately beforehand). This could explain some of the differences in performance of the GIRF-prediction in different subjects analyzed.

Concurrent monitoring allows capturing dynamic effects over the course of the fMRI experiment. These can be divided into two components, (a) non-LTI effects such as fluctuations caused by the subject, (b) changes in the GIRF over time. The latter could be addressed by measuring temperature dependent GIRFs (Nussbaum et al., 2018)(Stich et al., 2019). The hardware temperature can easily be assessed via the scanner's temperature monitoring system or using separate temperature sensors and this information can then be used to select the optimal GIRF for each measurement. Non-linear effects and fast-changing time-dependencies cannot be captured using this model. Concurrent monitoring of the encoding fields would have to be performed to correct for these effects.

In this study the reconstructions using measured trajectories provided the best results but concurrent monitoring is technically challenging and can be difficult to incorporate into routine fMRI scanning. When concurrent monitoring is not feasible GIRF-predicted trajectories provide an alternative. To concurrently monitor the long readouts required for high-resolution single-shot spirals field probes with suitable specifications (size and material (doping) of the probe) need to be chosen to avoid probe de-phasing during the measurement. If the optimal field monitoring setup is not available or if de-phasing still occurs (for example due to a poor shim) concurrent monitoring could be combined with GIRF-prediction, where the earlier part of the readout is measured and the later part is predicted(Wilm et al., 2019).

GIRF characterization is a one-time calibration step (previous work has shown the GIRF to be

stable over at least 3 years (Vannesjo et al., 2016)) and can be performed without any specialized equipment. In this study the GIRF was determined using a dynamic field camera, which allows very accurate characterization of the encoding fields with high frequency resolution (including accurately determining cross terms and higher order terms). However the GIRF can also be measured using a phantom-based approach (Addy et al., 2012; Duyn et al., 1998) with some loss in the frequency resolution of the GIRF (Graedel et al., 2017).

We used a spiral-out fMRI protocol for this study, but the GIRF-based trajectory prediction can be used for any trajectory. For example it could be employed for hybrid spiral-in/out methods (Glover and Law, 2001), which can provide high BOLD sensitivity as well as improved signal dropout artifacts. Beyond spirals the GIRF could enable other non-Cartesian fMRI techniques, which require accurate gradient correction, such as radial (G. R. Lee et al., 2010), PROPELLER (Krämer et al., 2012) and TURBINE fMRI (Graedel et al., 2016). Furthermore, the approach presented here is also useful to correct EPI trajectories, as the GIRF correction captures effects, which the commonly used odd-even lines EPI Nyquist ghost correction schemes (Schmitt et al., 1998) do not correct (Vannesjo et al., 2016).

# Conclusion

GIRF-predicted trajectories have the potential to enable high-quality spiral fMRI in situations where concurrent monitoring is not available. The presented approach requires only a one-time calibration per system, thus the fMRI acquisition is not prolonged or complicated by the acquisition of additional data for correction purposes.

# Acknowledgments

We would like to thank the Oxford-Brain@McGill-ZNZ Partnership in the Neurosciences for funding this project. Additionally, this work was supported by the Marie Curie Fellowship (J.V.), the NCCR “Neural Plasticity and Repair” (L.K) and the Wellcome Trust (N.G./J.V.). Technical support from Philips Healthcare is gratefully acknowledged

# References

Addy, N.O., Wu, H.H., Nishimura, D.G., 2012. Simple method for MR gradient system characterization and k-space trajectory estimation. Magn Reson Med 68, 120–129. doi:10.1002/mrm.23217

Andersson, J.L.R., Skare, S., Ashburner, J., 2003. How to correct susceptibility distortions in spin-echo echo-planar images: application to diffusion tensor imaging. Neuroimage 20, 870–888. doi:10.1016/S1053-8119(03)00336-7

Barmet, C., De Zanche, N., Pruessmann, K.P., 2008. Spatiotemporal magnetic field monitoring for MR. Magn Reson Med 60, 187–197. doi:10.1002/mrm.21603

Börnert, P., Schomberg, H., Aldefeld, B., Groen, J., 1999. Improvements in spiral MR imaging. Magn Reson Mater Phy 9, 29–41. doi:10.1007/BF02634590

De Zanche, N., Barmet, C., Nordmeyer-Massner, J.A., Pruessmann, K.P., 2008. NMR probes for measuring magnetic fields and field dynamics in MR systems. Magn Reson Med 60, 176–186. doi:10.1002/mrm.21624

Dietrich, B.E., Brunner, D.O., Wilm, B.J., Barmet, C., Gross, S., Kasper, L., Haeberlin, M., Schmid, T., Vannesjo, S.J., Pruessmann, K.P., 2016. A field camera for MR sequence monitoring and system analysis. Magn Reson Med 75, 1831–1840. doi:10.1002/mrm.25770

Duyn, J.H., Yang, Y., Frank, J.A., van der Veen, J.W., 1998. Simple correction method for k-space trajectory deviations in MRI. J. Magn. Reson. 132, 150–153. doi:10.1006/jmre.1998.1396

Eickhoff, S.B., Stephan, K.E., Mohlberg, H., Grefkes, C., Fink, G.R., Amunts, K., Zilles, K., 2005. A new SPM toolbox for combining probabilistic cytoarchitectonic maps and functional imaging data. Neuroimage 25, 1325–1335. doi:10.1016/j.neuroimage.2004.12.034

Engel, M., Kasper, L., Barmet, C., Schmid, T., Vionnet, L., Wilm, B., Pruessmann, K.P., 2018. Single-shot spiral imaging at 7 T. Magn Reson Med 80, 1836–1846. doi:10.1002/mrm.27176

Glover, G.H., 2012. Spiral imaging in fMRI. Neuroimage 62, 706–712. doi:10.1016/j.neuroimage.2011.10.039

Glover, G.H., Law, C.S., 2001. Spiral-in/out BOLD fMRI for increased SNR and reduced susceptibility artifacts 46, 515–522. doi:10.1002/mrm.1222

Glover, G.H., Lee, A.T., 1995. Motion artifacts in fMRI: comparison of 2DFT with PR and spiral scan methods. Magn Reson Med 33, 624–635.

Graedel N.N., Hurley S.A., Clare S., Miller K.L., Pruessmann K.P., Vannesjo S.J. 2017. Comparison of gradient impulse response functions measured with a dynamic field camera and a phantom-based technique. Proceedings of ESMRMB. No. 378

Graedel, N.N., McNab, J.A., Chiew, M., Miller, K.L., 2016. Motion correction for functional MRI with three-dimensional hybrid radial-Cartesian EPI. Magn Reson Med. doi:10.1002/mrm.26390

Jenkinson, M., Beckmann, C.F., Behrens, T.E.J., Woolrich, M.W., Smith, S.M., 2012. FSL. Neuroimage 62, 782–790. doi:10.1016/j.neuroimage.2011.09.015

Kasper, L., Engel, M., Barmet, C., Häberlin, M., Wilm, B.J., Dietrich, B.E., Schmid, T., Gross, S., Brunner, D.O., Stephan, K.E., Pruessmann, K.P., 2018. Rapid anatomical brain imaging using spiral acquisition and an expanded signal model. Neuroimage 168, 88–100. doi:10.1016/j.neuroimage.2017.07.062

Kasper L., Barmet C., Engel M., Heinzle J., Wilm B., Schmid T., Stephan K.E., Pruessmann K.P. 2017. Single-shot Spiral fMRI at 7 T with High Resolution and Geometric Fidelity. Proceedings of OHBM. No152

Kasper L., Engel M., Heinzle J., Mueller-Schrader M., Reber J., Schmid T., Barmet C., Wilm B.J., Schmid T., Stephan K.E., Pruessmann K.P. 2019. Advances in Spiral fMRI: A High-resolution Study with Single-shot Acquisition. BiorXiv

Kasper, L., Häberlin, M., Dietrich, B.E., Gross, S., Barmet, C., Wilm, B.J., Vannesjo, S.J., Brunner, D.O., Ruff, C.C., Stephan, K.E., Pruessmann, K.P., 2014. Matched-filter acquisition for BOLD fMRI. Neuroimage 100, 145–160. doi:10.1016/j.neuroimage.2014.05.024

Krämer, M., Jochimsen, T.H., Reichenbach, J.R., 2012. Functional magnetic resonance imaging using PROPELLER-EPI. Magn Reson Med 68, 140–151. doi:10.1002/mrm.23220

Lee, G.R., Griswold, M.A., Tkach, J.A., 2010. Rapid 3D radial multi-echo functional magnetic resonance imaging. Neuroimage 52, 1428–1443. doi:10.1016/j.neuroimage.2010.05.004

Lustig, M., Kim, S.-J., Pauly, J.M., 2008. A fast method for designing time-optimal gradient waveforms for arbitrary k-space trajectories. IEEE Trans Med Imaging 27, 866–873. doi:10.1109/TMI.2008.922699

Noll, D.C., Cohen, J.D., Meyer, C.H., Schneider, W., 1995. Spiral K-space MR imaging of cortical activation. J. Magn. Reson. Imaging 5, 49–56.

Nussbaum J., Wilm B.J., Dietrich B.E., Pruessmann K.P. 2018. Improved thermal modelling and prediction of gradient response using sensor placement guided by infrared photography. Proc Int Soc Magn Reson Med Sci Meet Exhib, p. 4210.

Pruessmann, K.P., Weiger, M., Börnert, P., Boesiger, P., 2001. Advances in sensitivity encoding with arbitrary k-space trajectories. Magn Reson Med 46, 638–651.

Schmitt, F., Stehling, M.K., Turner, R., 1998. Echo-Planar Imaging. Springer.

Smith, S.M., Jenkinson, M., Woolrich, M.W., Beckmann, C.F., Behrens, T.E.J., Johansen-Berg, H., Bannister, P.R., De Luca, M., Drobnjak, I., Flitney, D.E., Niazy, R.K., Saunders, J., Vickers, J., Zhang, Y., De Stefano, N., Brady, J.M., Matthews, P.M., 2004. Advances in functional and structural MR image analysis and implementation as FSL. Neuroimage 23 Suppl 1, S208–19. doi:10.1016/j.neuroimage.2004.07.051

Stich, M., Pfaff, C., Wech, T., Slawig, A., Ruyters, G., Dewdney, A., Ringler, R., Köstler, H., 2019. Temperature-dependent gradient system response. Magn Reson Med 44, 532. doi:10.1002/mrm.28013

Sutton, B.P., Noll, D.C., Fessler, J.A., 2003. Fast, Iterative Image Reconstruction for MRI in the Presence of Field Inhomogeneities. IEEE Trans Med Imaging 22, 178–188.

Vannesjo, S.J., Graedel, N.N., Kasper, L., Gross, S., Busch, J., Haeberlin, M., Barmet, C., Pruessmann, K.P., 2016. Image reconstruction using a gradient impulse response model for trajectory prediction. Magn Reson Med 76, 45–58. doi:10.1002/mrm.25841

Vannesjo, S.J., Haeberlin, M., Kasper, L., Pavan, M., Wilm, B.J., Barmet, C., Pruessmann, K.P., 2013. Gradient system characterization by impulse response measurements with a dynamic field camera. Magn Reson Med 69, 583–593. doi:10.1002/mrm.24263

Warnking, J., Dojat, M., Guérin-Dugué, A., Delon-Martin, C., Olympieff, S., Richard, N., Chéhikian, A., Segebarth, C., 2002. fMRI retinotopic mapping--step by step. Neuroimage 17, 1665–1683.

Wilm, B.J., Barmet, C., Gross, S., Kasper, L., Vannesjo, S.J., Haeberlin, M., Dietrich, B.E., Brunner, D.O., Schmid, T., Pruessmann, K.P., 2016. Single-shot spiral imaging enabled by an expanded encoding model: Demonstration in diffusion MRI. Magn Reson Med 77, 83–91. doi:10.1002/mrm.26493

Wilm, B.J., Dietrich, B.E., Reber, J., Vannesjo, S.J., Pruessmann, K.P., 2019. Gradient response harvesting for continuous system characterization during MR sequences. IEEE Trans Med Imaging 1–1. doi:10.1109/TMI.2019.2936107

Wright, K.L., Hamilton, J.I., Griswold, M.A., Gulani, V., Seiberlich, N., 2014. Non-Cartesian parallel imaging reconstruction. J. Magn. Reson. Imaging 40, n/a–n/a. doi:10.1002/jmri.24521

Yang, Y., Glover, G.H., van Gelderen, P., Patel, A.C., Mattay, V.S., Frank, J.A., Duyn, J.H., 1998. A comparison of fast MR scan techniques for cerebral activation studies at 1.5 tesla. Magn Reson Med 39, 61–67.

Spirig Y., Graedel N.N., Kasper L., Miller K.L., Frost R., Clare S., Pruessmann K.P. 2017. Interaction between trajectory deviations and B0 field inhomogeneity in readout-segmented EPI and spiral imaging. Proc Int Soc Magn Reson Med Sci Meet Exhib, p. 3917.

Zhang, Y., 0001, M.B., Smith, S.M., 2001. Segmentation of Brain MR Images through a Hidden Markov Random Field Model and the Expectation Maximization Algorithm. IEEE Trans Med Imaging 20, 45–57. doi:10.1109/42.906424

Zilles, K., Amunts, K., 2010. Centenary of Brodmann's map--conception and fate., Nature reviews. Neuroscience. Nature Publishing Group. doi:10.1038/nrn2776